Multiple rock-slope failures from Mannen in Romsdal Valley, western Norway, revealed from Quaternary geological mapping and ^{10}Be exposure dating

PAULA HILGER*†, REGINALD L. HERMANNS*‡, JOHN C. GOSSE#, BENJAMIN JACOBS◇, BERND ETZELMÜLLER†, MICHAEL KRAUTBLATTER◇

* Geohazards and Earth Observation, Geological Survey of Norway, N-7491 Trondheim, Norway
† Department of Geosciences, University of Oslo, N-0316 Oslo, Norway
‡ Department of Geoscience and Petroleum, Norwegian University of Science and Technology, N-7491 Trondheim, Norway
# Department of Earth Sciences, Dalhousie University, B3H 4R2 Halifax, Canada
◇ Department of Civil, Geo and Environmental Engineering, Technical University of Munich, D-80333 Munich, Germany

Abstract

Oversteepened valley walls in western Norway have high recurrences of Holocene rock-slope failure activity causing significant risk to communities and infrastructure. Deposits from six to nine catastrophic rock-slope failure (CRSF) events are preserved at the base of the Mannen rock-slope instability in the Romsdal Valley, western Norway. The timing of these CRSF events was determined by terrestrial cosmogenic nuclide dating and relative chronology due to mapping Quaternary deposits. The stratigraphical chronology indicates that three of the CRSF events occurred between 12 and 10 ka, during regional deglaciation. Congruent with previous investigations, these events are attributed to the debuttressing effect experienced by steep-slopes following deglaciation, during a period of paraglacial relaxation. The remaining 3-6 CRSF events cluster at 4.9 ± 0.6 ka (based on 10 cosmogenic ^{10}Be samples from boulders). CRSF events during this later period are ascribed to climatic changes at the end of the Holocene thermal optimum, including increased precipitation rates, high air temperatures and the associated degradation of permafrost in rock-slope faces. Geomorphological mapping and sedimentological analyses further permit the contextualization of these deposits within the overall sequence of post-glacial fjord-valley infilling. In the light of contemporary climate change, the relationship between CRSF frequency, precipitation, air temperature, and permafrost degradation may be of interest to others working or operating in comparable settings.

Keywords: Rockslides, cosmogenic ^{10}Be dating, cluster, debuttressing, climate change, fjord-valley infill

1. Introduction

Formerly glaciated valleys often exhibit slope instabilities that lead to catastrophic rock-slope failures (CRSF) (e.g. Hermanns and Longva, 2012). Though CRSF are often attributed to seismic activity (e.g. Korup, 2004; Hewitt et al., 2008; Agliardi et al., 2009; Penna et al., 2011; Moreiras et al., 2015), many are triggered by climatogenic destabilisations owing to post-glacial debuttressing, permafrost degradation, or precipitation increases (Evans and Clague, 1994; Trauth et al., 2000; Soldati et al., 2004). Deglaciation and valley adjustment in the Lateglacial and Holocene provoke localised stress concentrations in steep fjord rock walls exceeding the crack initiation threshold; coincidently advancing and retreating permafrost significantly alters rock mass strength properties (Leith et al., 2014; Krautblatter and Leith, 2015). Both, in situ stress evolution and rapidly changing material strength due to permafrost advance play a key role in controlling rock slope failure evolution. Changing permafrost conditions alter the strength of (i) intact rock, (ii) ice infill and (iii) rock ice interfaces by 20-80% and freezing causes high cryostatic stresses and irreversible rock fatigue (Krautblatter et al., 2013; Jia et al., 2015; Jia et al., in press). Previous studies from Scotland and Norway indicate that CRSF commonly occur within the first 2 ka of deglaciation (Holm et al., 2004; Cossart et al., 2008; Ballantyne and Stone, 2013). Events within this time window are commonly attributed to "debuttressing" – the unloading and stress release experienced in paraglacial environments following deglaciation, although it is difficult to preclude seismicity caused by post-glacial isostatic adjustment. CRSF occurring outside of this interval are often attributed to changing climate, in particular higher precipitation rates, air temperatures, and, in some cases, permafrost degradation (Fischer et al., 2006; Allen et al., 2009; Krautblatter et al., 2013; Nagelisen et al., 2015). The temporal and spatial distribution of CRSF in Norway reflects the strong influence of debuttressing on slope stability. However, continued rock-slope activity throughout the Holocene has also been identified (Blikra et al., 2006; Hermanns et al., 2017). Few studies have investigated the relation between climatic variability and CRSF frequency in Norway (Blikra and Christiansen, 2014; Böhme et al., 2015).

A precise geochronology is necessary to establish cause and assess hazard of CRSF which may have recurrences exceeding millennia. Until the late 90s, most CRSF event chronologies relied on independently-dated stratigraphically-related sediments for limiting or contemporaneous age control (e.g. Topping, 1993; Clavero et al., 2002). For post-glacial events radiocarbon dating was frequently used (Hermanns et al., 2000; Orwin et al., 2004; Ostermann et al., 2016). Recently, terrestrial cosmogenic nuclide (TCN) exposure dating is more frequently used to directly date CRSF deposits (Gosse and Phillips, 2001; Ivy-Ochs and Kober, 2008; Sturzenegger et al., 2015; Ostermann et al., 2017). Recent studies have utilized TCN methods to determine the timing of CRSF events and better relate them to otherwise hypothetical triggering mechanisms (e.g. Ballantyne et al., 1998; Hermanns et al., 2004; Dortch et al., 2009; Hermanns et al., 2015). However, in most mountain environments the limited number of investigations precludes a comprehensive assessment of the conditioning variables

that lead to failure. Exceptions exist for the European Alps, Scotland and Norway where many studies have been conducted (e.g. Ballantyne et al., 2014; Hermanns et al., 2017; Ivy-Ochs et al., 2017).

The rock-slope instability "*Mannen*" in Romsdal Valley, Norway is located in a key region for tourism, and is situated above the farming community of Marstein. The risk of rock-slope failure at Mannen has been considered high owing to geological structural preconditioning and observed deformation and sliding rates of cliff blocks. In this region, the recurrence interval for a 0.15 Mm^3 failure is estimated to be <100 years while the recurrence of a 2-4 Mm^3 volume is 100 to 1000 years (Blikra et al., 2016). Extensive CRSF deposits with volumes between 0.05 and 1.95 Mm^3 from previous events have accumulated in the valley bottom beneath Mannen. It is therefore important to decipher the frequency of previous failures in order to assess if historic CRSF events were randomly distributed or clustered in time and if they can be linked to a particular failure mechanism. Using techniques of Quaternary geological mapping, sedimentary stratigraphy, electrical resistivity tomography (ERT), ground penetrating radar (GPR), and cosmogenic ^{10}Be exposure dating we (1) determine the timing of post-glacial CRSF events at Mannen, (2) contextualize the colluvium within the framework of a fjord-valley fill succession, and (3) identify the antecedent climate and glacially-generating conditions resulting in periods of heightened CRSF activity.

2. Setting

Mannen is situated along a north facing slope of the glacially formed, U-shaped Romsdal Valley (Fig. 1; 62.46°N, 7.77°E; Møre og Romsdal, Norway). This lower reach of the valley is a fjord-valley, or sediment-filled palaeofjord (Corner, 2006) with an underfit stream. Within 10 km of the site, the valley walls reach between 800 m and 1400 m above the valley floor. The rock-slope section at Mannen is 1295 m in height with an average slope gradient of 47°. At present, there are four active rock-slope instabilities along the southern and south-western slope of the lower Romsdal Valley (Saintot et al., 2012). Each site is situated above massive rock-avalanche and debris-flow deposits on the valley floor (Fig. 1).

[Fig. 1]

Mannen is located in the Western Gneiss Region, which consists of Precambrian crystalline basement rocks of the Scandinavian Caledonides (Roberts, 2003). The Romsdal Valley cuts east-west through dioritic-granitic gneiss with local transitions to quartz-rich gneiss with sillimanite and kyanite and coarse granitic gneiss (Tveten et al., 1998). The Caledonide structural fabrics and mineralogical banding impart critical weaknesses inherent along the glacially oversteepened valley sides.

Here, post-Weichselian deglaciation began by thinning during the Bølling/Allerød interstadial (ca. 15-13 ka), as the outer coast of western Norway became ice-free (Longva et al., 2009). Ice marginal retreat up the Romsdal Valley has been completed between 12.8 and 11.7 ka, following the Younger

Dryas cold period (Hughes et al., 2016; Stroeven et al., 2016; Hermanns et al., 2017). During deglaciation, the landscape was inundated by the sea, reaching a marine limit of 120 m above modern sea level in the Romsdal Valley (Høgaas et al., 2012) (i.e. 60 m above the Rauma River at Mannen). Subsequently the relative sea level lowered approximately exponentially with glacioisostatic uplift (Svendsen and Mangerud, 1987).

The Quaternary valley infill is the product of processes connected to the Pleistocene glaciation, post-glacial sea-level fall and paraglacial colluvial activity (Fig. 1). The geomorphology of the Mannen area in the lower Romsdal Valley is dominated by talus, debris-flow cones, and CRSF deposits (Fig.1; Blikra et al., 2006; Saintot et al., 2012). More than 30 historical mass wasting events are documented along the valley (NVE, 2018), dominated by small rock-fall events with a volume <100 m^3. Relative to the sea-level history, these deposits stratigraphically post-date ice marginal retreat with varying failure timing throughout the Holocene (Blikra et al., 2006).

The mean annual air temperature ranges from 4°C in the valley bottom to -1.5°C on the plateau above Mannen (1300 m a.s.l.). Annual precipitation during the reference period 1961-1990 lies between 1000 and 1500 mm in the Romsdal Valley. During the winter season, the snow precipitation accumulates an average of 37 cm of snow cover with monthly means of 12-25 cm in November and Mai and 50-56 cm in December and January. During the last 20 years the values have increased slightly, now usually being close to the upper limits of these ranges. Temperatures have increased as well, particularly since the year 2000 with 1°C in relation to the last reference period 1961-1990 (NVE, met.no and Kartverket, 2018).

3. Methods

3.1 Quaternary geological mapping

High-resolution (1 m and 5 m) bare-earth LiDAR-derived digital elevation models (DEM) are the main sources for the recognition of landforms (e.g. Schleier et al., 2016). The digital relief analysis was complemented by field mapping in the summers 2016 and 2017 on the area around Mannen but included a ca. 40 km region extending from the contemporary fjord-head delta to the Skiri rock avalanche (Fig. 1). Landform elevations were extracted from the DEM and plotted together with the local relative sea-level curve in order to establish the relationships between the marine transgression and regression and the onshore stratigraphy (c.f. Eilertsen et al., 2015). Small excavations and field observations of the sediment characteristics facilitate the classification of different surface levels along the entire Romsdal Valley. The sedimentology characterisations and interpretations are based on field observations, GIS analyses, and previous studies about typical valley-fill stratigraphy in Norwegian fjord valley settings (c.f. Corner, 2006; Eilertsen et al., 2006).

The volume of the CRSF deposits was estimated by reconstructing the pre-failure surface from the most recent high-resolution (1 m) LiDAR data. Based on interpolated and modified 5-m contour lines

we created new pre-failure DEM, which were then used to extract the elevation differences and subsequently calculate the volume on a pixel basis.

Two 2D ERT profiles, 900 m and 700 m in length and parallel to the valley axis, were obtained on the northern and southern sides of the Rauma River (Fig. 1B). ERT utilized an ABEM Terrameter LS (ABEM, 2016) and field testing employed the roll-along method using the Schlumberger protocol (e.g. Aizebeokhai, 2010) with four 100 m long cables and 5 m electrode spacing. To interpret the subsurface geology, the inverse electrical conductivity was derived with RES2DINV (© M.H.Loke, 1995-2015). After the manual extermination of bad data points, the inversion was derived using the robust L_1-norm.

A single ground-penetrating radar (GPR) profile was conducted, running along the foot of the valley parallel 20m-step in the relief in the north-west of the study site (Fig. 1B). We used a snake antenna with a frequency of 100 MHz, which was towed behind the surveyor. The measurement frequency was 0.5 m. The post-processing was conducted with RadExplorer (© MALÅ Geoscience).

3.2 Geochronology

Thirteen samples were collected and processed for surface exposure dating with cosmogenic ^{10}Be in quartz. We sampled boulders representing at least four of the CRSF deposits below the Mannen rock-slope instability. The boulders are well distributed and their sampled surfaces lie more than 1 m above the surroundings and have an either flat or convex geometry. All samples were taken with hammer and chisel and are 1-6 cm thick (Table 1). Where the foliation was favourable the collected samples have a rather even thickness of 2-3 cm and 20-30 cm of diameter. Generally, the selected sample locations on the CRSF deposits are either on flat or convex boulder surfaces with at least 40 cm distance to the boulder edge to minimize the effect of neutron loss and local shielding. In two cases the samples are only 20 cm from the boulder edge (MANN-31 and -38) and three samples are collected from boulder surfaces steeper than 30° (MANN-23, -32 and -35). Most sampled boulders were in discontinuous boulder fields with deep interstitial gaps, lacking the infill of a finer matrix(Fig. 2A-C). Many boulders were covered by up to five-centimetre thick moss with a (dry) density of 0.05 g cm^{-3}. An open birch forest with 5-20 cm trunk diameter and 2-12 m height covers the CRSF deposits today, with solitary pine trees in places.

181 Table 1: sample characteristics, the boulder height refers to the surrounding ground or boulders

Sample name	Rock type	Sample thickness [cm (estimated average)]	Orientation (dip direction/dip)	Boulder dimensions (a- & b-axis) [m]	Boulder (sample) height [m]	Shortest distance to edge [cm]	Moss [cm]
MANN-07	Medium/coarse grained granite	1	264/20	2x4	3	100	3
MANN-10	Medium/coarse grained gneiss	2.0-4.0 (2.5)	302/10	5x5	3	50	5
MANN-23	Medium/coarse pophyrytic granite	5	074/30	1x2	1	convex boulder	-
MANN-26	Fine grained micaceous gneiss	3	000/20	15x7	7	70	3
MANN-28	Fine grained felsic gneiss	3.0-6.0	234/10	4x3	2.5	50	4
MANN-31	Medium grained, strongly foliated gneiss	0.5-5.0 (3.5)	358/36	1.5x1.5	3	20	1
MANN-32	Fine grained gneiss	1.0-5.0 (4.0)	254/18; 149/49	12x3.5	2	convex boulder	0.5
MANN-35	Medium/coarse grained granitic gneiss	2.5	181/32	7x6	2.5	300	-
MANN-36	Medium grained strongly foliated gneiss	2.5	315/12	4x3	2.5	150	4
MANN-37	Weakly foliated granitic gneiss	1.0-2.0 (1.5)	071/26	8x6	8	300	4
MANN-38	Fine grained gneiss with mid-strength foliation	1.0-6.0 (5.0)	084/20	5x2	1.5	20	-
MANN-39	Medium grained gneiss with mid-strength foliation	1.0-2.0 (2.0)	132/26	5x2	1.5	40	2
MANN-40	Fine grained and weakly foliated gneiss	1.0-5.0 (4.0)	305/15	2.5x2	1	50	5

182

183 [Fig. 2]

184

185 Selected samples were cleaned by brushing, crushed, ground and sieved, optimizing the 250-
186 355 μm fraction. We subsequently concentrated and purified the quartz at the Cosmic Ray Isotope
187 Sciences at Dalhousie University (CRISDal) lab, Halifax, Canada, using magnetic separation, froth
188 flotation, heavy liquid separation, and chemical leaching. The abundance of selected cations including
189 Be were measured with ICP-OES at CRISDal to ensure purity (<100 ppm Al and Ti). Following
190 carrier addition (240 mg of Be) to 30 g of pure quartz for each sample, the samples were digested in a
191 mixture of concentrated trace-metal grade perchloric, hydrofluoric, and aqua regia. Be-Carrier-B31
192 was produced at CRISDal on Sept 28, 2012 from a deeply sourced Ural Mountains phenacite with low
193 levels of ^{10}Be (averaging 150 atoms ^{10}Be per mg ^{9}Be over multiple years, e.g. ^{10}Be/^{9}Be of the carrier
194 averaging 10^{-17} and lower, usually with zero or one counts over 400 s with 20 μAmp current at
195 Lawrence Livermore National Lab. The Be concentration of the carrier was determined by ICP-OES
196 at CRISDal and by ICP-OES at PRIME Lab to be 282 ± 5 μg/ml with a density of 1.013 g/ml, and this
197 2% uncertainty is included in the total analytical error of each measurement). Following routine
198 column chemistry with sulfination, pH controlled precipitations with ammonia gas, and calcination to
199 BeO over a bunsen burner flame, the BeO was pulverized in its low-boron quartz vial and mixed well
200 with niobium powder (1:1.5 BeO:Nb by volume). The prepared targets were measured by accelerator

mass spectrometry (AMS) at Lawrence Livermore National Laboratory, Livermore (USA) against standard 07KNSTD-3110 ($^{10}Be/^{9}Be$ $2.85x10^{-12}$) and achieved 2-3% AMS precision on most samples. The process blank correction ($5.59*10^{3}$ atoms, $^{10}Be/^{9}Be$ $3.3x10^{-16}$, which is very close to the average blank since 2016) resulted in the subtraction of <1% of the measured concentrations.

To estimate the topographic shielding we measured with an inclinometer the azimuth and gradient to several skyline inflection points. As low-level clouds and vegetation affected some measurements, the shielding correction was verified with a high resolution (5-m) DEM. For this, the elevation for each sample was corrected using the LiDAR data and the angle to the horizon derived for each azimuth. These values are on average 1.3˚ higher than the correspondent inclinometer measurements but have a much higher resolution and should thus overall be more accurate. Snow shielding was derived after Gosse and Phillips (2001) using historic and modern climate data to estimate the average seasonal snow cover (snow density ~0.3 g cm^{-3}). This method only represents the snow cover for the last decades and does not include local effects such as vegetation and wind drift. An erosion rate of 1 mm ka^{-1} was used for the calculation (Zimmerman et al., 1994). For the calculation of the exposure ages we used version 3 of the online exposure age calculator formerly known as the CRONUS-Earth online exposure age calculator written by G. Balco, 2017, and the LSDn scaling scheme.The reported 1σ uncertainty for an exposure age includes the internal and external errors (details in supplementary files).

4. Results

4.1 Quaternary geology and geomorphology

Geomorphological mapping using high-resolution (1 m) LiDAR data - The digital elevation model revealed well defined 20 m high steps in the relief on both sides of the valley below the Mannen rock-slope instability (transition from green to yellow colouring in Fig. 1B; an additional plain hillshade-map can be found in the supplementary files for comparison). The steep slopes with angles around 35˚ run almost parallel to the Rauma river and are connected to rather flat (<5˚) elevated surfaces. Upstream, these elevated surfaces end abruptly, where the steep slopes turn towards the rockwalls. These stepped landforms are overlain by at least five but possibly up to seven lobate CRSF deposits. While one of these mapped CRSF events, featuring a secondary failure scar, has overrun and modified the steep 20 m high slope, the latter draws through most of the other CRSF deposits. A lobate and hammocky landform on a low elevation basin-like section north-east of the high elevated landforms suggest up to two additional CRSF deposits. A third larger event, exceeding the Rauma River, has been mapped by an intensive GPR survey (Tønnesen, 2009). But since the deposits of this event are no longer visible at the surface, it was not possible to include them into the age determinations of this study.

[Fig. 3]

Longitudinal valley profile and terrace mapping – The valley-fill deposits along the Rauma Valley were mapped in relation to the longitudinal profile of the Rauma River (Fig. 3). The terraced landforms below the Mannen rock-slope instability are the highest valley fill deposits along the Romsdal Valley, exceeding all other valley-fill sediments by more than 10 m. The next highest terraces have been investigated with small (~1m deep) excavations along the entire valley (Fig. 1A). They revealed coarse sand interbedded with fine sand with 1-50 cm large rounded to well rounded clasts in the upper Romsdal Valley (Fig. 3A+B) and patterns of altering sand layers of varying grain sizes without pebbles and cobbles close to the fjord head. The bedded structure and clast roundness imply fluvial deposition processes but because of their high elevations, these terraces are interpreted to be of glacio-fluvial origin, which is in accordance with the most recent regional quaternary geological map (NGU, 2018). High elevated sand deposits with nearly horizontal sandy layers are found on either side of the valley in bay-like settings (Fig. 3C) and have previously been interpreted as beach deposits (NGU, 2018). The correlating elevation of these beach deposits and the sandy terrace segments covering large parts of the lower Romsdal Valley (Fig. 1A) suggests a possible deposition of distal fine grained glacio-fluvial sediments in a deltaic environment and thus indicating the sea-level at the time of deposition.

Sedimentary stratigraphy and interpretation below the Mannen rock-slope instability - The upper ca. 40 m of the fjord-valley fill below the Mannen instability was investigated in three locations (A-C; Fig. 1B). Four sedimentary facies associations (FA I-IV) are identified and likely relate to the progradation of a fjord-head delta system and its associated braided river, rock-slope failure and related processes, including debris flows on colluvial fans. A brief tabular summary of the following sections is provided in the supplementary files.

FA I stratigraphically occupies the lowermost position at the locations A and B (Fig. 4). Observed exposures were ca. 22 m in height. FA I consists of stratified sands and gravels, which dip ca. 5° in downstream direction (Fig. 4A). Gravel clasts are typically subrounded to rounded. FA I is interpreted to be stratified drift. Similar units of stratified drift consisting of sands and gravels, are frequently described in fjord-valleys in western Norway (c.f. Corner, 2006). Considering the high relative elevation of these sediments together with their morphological appearance connected to a steep slope facing upstream and downstream dipping sediment layers FA I could be interpreted to represent an ice-contact glaciomarine fan or delta (c.f. Lønne, 1995; Corner, 2006; Eilertsen et al., 2006).

[Fig. 4]

FA II is observed overlying FA I at location A (Fig. 1). The deposits are ca. 5 m thick and consist of flat-laying interbedded silty sands and gravels. Gravel clasts are angular to sub-angular. Variations

in clast shape reflect changes in the transport distance and sediment source. Angular clasts likely entered the fluvial domain as debris flows from the proximal upstream reaches and hence were transported a short distance prior to deposition. Based on the sedimentary architecture and composition, FA II is interpreted to be fluvial with debris-flow deposits, deposited on the distal parts of colluvial fans (c.f. Blikra and Nemec, 1998).

FA III is encountered at locations B and C (Fig. 1) and varies from ca. 8 to >10 m in thickness. Deposits consist of boulders (up to 10 m in diameter) as chaotic block fields or suspended in a gravelly, sandy matrix covered with soil (Fig. 4B). FA III is interpreted as catastrophic rock-slope failure deposits.

FA IV is observed in the upper 7 m at location C. The deposits consist of interlaminated sands and silts (Fig. 4C). Isolated, sub-angular to angular, cobble-size fragments are incorporated within FA IV. FA IV is tentatively interpreted as overbank fluvial deposits (c.f. Corner, 2006; Eilertsen et al., 2006) with outsized cobbles being debris originating from a steep, proximal slope (Blikra and Nemec, 1998). If so FA IV is an indicator for a higher water level than today's river level at time of deposition.

[Fig. 5]

Direct current (DC) resistivity - The tomography of the ERT profiles (Fig. 1) generally support our sedimentological and geomorphological observations. Based on the 2D distribution of the electrical resistivity of the profiles ERT (A) and B we defined five main electrical resistivity units (ERU): ERU 0, I, II and III, with ERU I, II and III corresponding to FA I, II and III, respectively.

ERU 0 occupies the lower 40 m of both DC resistivity profiles (Fig. 5 A+B). The unit is characterised by resistivity values from <400 Ωm to 5 kΩm and a transition to high resistivity values of > 14 kΩm at 50-60 m a.s.l. The elevation of this transition coincides with the lower limit of the mapped dry and coarse-grained stratified drift (FA I). However, we have no field information about sediment characteristics below this elevation. The similar resistivity patterns of the two profiles suggest that the bottom geologic characteristics are similar over the entire width of the Romsdal Valley. While the fjord-valley models would expect fine grained glaciomarine sediments at the valley bottom, the typical resistivity values for clays do not exceed 100 Ωm. We therefore suggest this lower unit to be either bedrock (Palacky, 1988), or inversion artifacts due to the high values above.

ERU I is characterised by resistivity values of 14 - >36 kΩm and occupies the largest parts of both sections ERT (A) and B. This unit lies above ERU 0 between ca. 50 and 90 m a.s.l. The highest values in ERT (A) are most likely an artefact due to the proximity of the edge to the open gravel pit. ERU I is interpreted to represent FA I with glacio-fluvial sand and gravels (Palacky, 1988).

ERU II occupies the upper 5-7 m in section ERT (A). Resistivity values range from 350 Ωm in the uppermost two meters to values above 14 kΩm. But the values are generally lower than in unit I. ERU II represents the sediments interbedded silty sand layers in debris-flow gravels of FA II. The variation

of the resistivity values are interpreted to originate from different sedimentation processes related to the talus cone above.

ERU III was only observed in section ERT (B). This unit is characterised by high values (>14 kΩm) at the top 2-5 m with lower values (5-14 kΩm) below this surface layer. At the letter f and g (Fig. 5B) CRSF deposits have been mapped in the field. The decrease of resistivity with depth can be explained by the typical grain-size distribution of massive CRSF deposits with large boulders on the surface and an increase in finer matrix material and moisture with depth (Ostermann et al., 2012). While the resistivity values are generally lower within the section c-d in the same profile, this unit is also correlated to FA III. Here, up to 20cm deep surface water was observed in the field indicating a high water content in the subsurface, leading to a decrease in the resistivity.

ERU IV occupies the last 100-200 m of the 900 m long ERT profile A (a-c; Fig. 5A), where the electrical resistivity values lie between 50 and 350 Ωm. This section of the profile is part of the basin upriver of the high-elevated valley-fill sediments below Mannen. We suggest this unit to be silty sediments deposited either in a calm water environment or as overbank fluvial deposits similar to FA IV (Groover et al., 2016).

Ground penetrating radar - The surface along most of the GPR profile (Fig. 1B and 5C) is characterised by agriculturally used lawn. A chaotic boulder field confining the Rauma River along this section generated a minor knickpoint in the longitudinal profile (Fig. 3), which is often the consequence of CRSF into rivers (Ouimet et al., 2007; Korup et al., 2010). The characteristic reflection configurations and analogies to the ERT units allowed defining four main radar units (RU): RU I-IV, where RU III and IV correspond to FA III and IV, respectively.

RU 0 is defined by an area below 45 m a.s.l. where the signal strength decreases abruptly and no clear reflectors are distinguishable. The upper limit of this unit lies only a few meter lower than the upper limit of ERU 0 (50-60 m a.s.l.) wherefore we interpret this unit tentatively as bedrock.

RU I is defined by a partly clear reflecting boundary, that can be followed throughout large parts of the profile (thick line Fig. 5C). This reflector becomes rather indistinct at the boundary to RU III and the reflectors within this unit are rather chaotic and unclear. Because of the lack of homogeneous reflectors we interpret this unit as valley-fill sediments that have been deformed by the impact of the CRSF (c.f. Blikra et al., 2006).

The RU II unit is characterised by steeply downstream dipping (35-45˚) generally parallel reflectors. Analog reflectors are commonly observed in deltaic environments (Eilertsen et al., 2011). Considering the fjord-valley setting we interpret RU II to represent delta foreset deposits, indicating a previous sea- or lake-level at ca. 55 m a.s.l.

RU III represents the central section of the GPR survey, where we observe distinguishable parable-shaped reflectors in different elevations. RU III is interpreted as CRSF deposits (FAIII) (c.f. Schleier et al., 2016), which can be observed at the surface only a few meters north-east of the profile.

The RU IV unit is characterised by smooth parallel and continuous horizontal reflectors with varying thickness. While these characteristics are common for stratified sediments, it is difficult to distinguish between different possible deposition processes. Similar reflectors have been observed for delta bottom/topsets (Eilertsen et al., 2011), lake deposits (Storms et al., 2012) and flood plains (Hansen et al., 2009). Because of its location and our field observations we interpret this unit as fluvial overbank flow sediments correlating with FA IV.

[Fig. 6]

Quaternary geological map –The Quaternary geology map displays the dominance of CRSF deposits and their position relative to the stratified drift. The volumes of the individual CRSF events vary between 0.05 (Lobe 5) and 1.95 Mm^3 (Lobe 4, Fig. 6). The small rock-slope failure Lobe 5 is characterised by a clast-supported chaotic block field with large angular boulders (3-6 m) and little to no matrix exposed at the surface. Considering its short run-out length, Lobe 5 probably represents a large rock-fall event without major disintegration. It exceeds the active extensive talus slope by >150 m. According to a previous GPR survey (Tønnesen, 2009) the CRSF deposits 6a and 6b are much larger than the superficial deposits indicate. The study suggests that the deposits continue below the Rauma River and that the volume is thus much larger than our estimated 0.43 Mm^3.

Table 2: Analytical data and calculated exposure ages with the LSDn scaling scheme. Shielding values include the topographic shielding as well as shielding by snow. Sample marked with * is defined as a statistical outlier.

Sample name	Latitude (dd)	Longitude (dd)	Alti-tude (masl)	^{10}Be Concen-tration (10^4 at/g)	1σ analytical unc. (10^4 at/g)	Shielding correc-tion	Age (ka)	Age unc. internal (ka)	Age unc. external (ka)	Lobe	Error weighted mean with int. (ext.) unc.
MANN-07	62.46503	7.793195	70	21.30	0.75	0.9128	4.75	0.12	0.33	**6b**	
MANN-10	62.46522	7.796929	63	22.00	0.69	0.9173	5	0.16	0.34		**4.95±0.1 (0.31)**
MANN-23	62.46579	7.795452	68	22.10	0.84	0.9152	5.12	0.2	0.36	**6a**	
MANN-26*	62.46529	7.795589	68	26.00	0.77	0.9165	5.93*	0.18	0.39		
MANN-31	62.46634	7.788837	111	22.80	0.80	0.9100	5.03	0.17	0.35	**5**	**4.96±0.15 (0.33)**
MANN-32	62.46655	7.788266	110	21.70	1.21	0.9084	4.81	0.18	0.39		
MANN-35	62.46807	7.786672	118	45.40	2.33	0.9059	9.92	0.27	0.79	**2**	**9.39±0.3 (0.64)**
MANN-36	62.46801	7.786364	117	41.80	1.69	0.9054	9.12	0.52	0.66		

MANN-28	62.46924	7.783871	138	23.40	0.79	0.9033	5.11	0.37	0.35		
MANN-37	62.47001	7.7864	95	21.10	0.69	0.8946	4.7	0.16	0.32		
MANN-38	62.47067	7.787071	88	21.60	0.82	0.8901	5.05	0.17	0.36	**4a**	**4.93±0.09 (0.30)**
MANN-39	62.47122	7.784973	78	21.20	0.73	0.8856	4.88	0.16	0.36		
MANN-40	62.47038	7.782797	117	22.30	0.75	0.8956	4.98	0.2	0.34	**4c**	

4.2 Geochronology

We have determined the apparent exposure ages of 13 boulder samples using the ^{10}Be-isotope (Fig. 6; Table 2). The locations of the two samples with the oldest apparent ^{10}Be ages are adjacent to each other and give a mean exposure age of 9.39 ± 0.64 ka (error-weighted mean with 1σ uncertainty). The majority of the deposit lies below the marine limit, and while only the highest boulders were sampled, shielding by seawater may have reduced the ^{10}Be production rate. Thus, assuming no inheritance, these dates are interpreted to be minimum limiting ages. The other eleven exposure ages range from 4.75 ± 0.33 ka to 5.93 ± 0.39 ka. Considering that sample MANN-26 as a statistical outlier (beyond the coefficient of variation of the mean of the others) owing possibly to inherited ^{10}Be isotopes from pre-failure production, the range is 4.75 ± 0.33 ka to 5.12 ± 0.36 ka and the ages are indistinguishable within their 1σ uncertainties. Excluding MANN-26, the mean ages for deposits 4a, 5 and 6 (Fig. 6) are 4.91 ± 0.30 ka, 4.96 ± 0.33 ka and 4.95 ± 0.31 ka, respectively. The single sample from Lobe 4c gives an age of 4.98 ± 0.34 ka, which lies within the standard deviation of Lobe 4a and, based on their close proximity and stratigraphic relationship, we recommend considering them as one event with a mean age of 4.93 ± 0.30 kain the following discussions. The clearly distinguishable deposits of several CRSF events with indistinguishable ages within one standard deviation indicate temporal cluster of multiple failures from the same slope 4.9 ± 0.6 ka ago.

Poor estimations of partial cosmic ray shielding by snow and vegetation provide an unconstrained source of error in our ages. Our shielding estimations for snow, with an average of 37 cm snow depth for a 7 month snow season and an average density of 0.3 g cm^{-3}, yielded a value of 0.999 which has a small effect on the absolute exposure ages. The effect of the sparse birch tree forest that covers the sampled CRSF deposits can roughly be estimated. Plug et al. (2007) show that the shielding effect in forests is dependent on stem thickness and tree height, sample location, succession rate, and age. Considering the generally small stem diameters (5-20 cm) and forest density we expect the shielding effect to be smaller than the numerically estimated shielding of < 2.25% for Acadian forest in Nova Scotia (Plug et al., 2007).

Potential inheritance of ^{10}Be in each boulder depends on its depth below the cliff face prior to failure and the rate of cliff retreat (frequency of mass wasting). The study area has relatively small CRSF volumes (0.05-1.95 Mm^3). For a conservative realistic scenario of 7 ka pre-failure exposure (4.9 ka subtracted from an exposure history of ~12 ka after deglaciation), the effect of inheritance for 10 m

and 5 m depth below the cliff face are ca. 0.8 and 1.5%, respectively (Hilger et al., unpublished data).However, the average effect becomes >6% for depths smaller 2 m. But because of the existence of an outlier (MANN-26), that possibly came from a depth < 2 m, and otherwise uniform ages, we expect most of the boulders came from greater depth. Because shielding by vegetation and inheritance impart opposite effects on exposure ages (decreasing or increasing apparent exposure time), and because they are of similar effect (a few %), and considering the tight distribution of the boulder exposure ages, it is possible that the two factors effectively cancel each other. Therefore we have not adjusted the ages for either factor, and interpret the measured exposure ages as the timing of the CRSF events.

5. Discussion

5.1 Timing of CRSF cluster from Mannen

Our study indicates multiple early post-glacial rockslide events, and a "geological crisis" during the mid-Holocene. Because of the high marine limit, the sampling of stratigraphically low deposits was restricted to boulders on higher elevations in the study site. Consequently, we are lacking absolute exposure ages for the CRSF deposits 1 and 3 and are dependent on geomorphologic and stratigraphic observations relative to the dated deposits. The geomorphological setting of the deposits clearly indicate that the CRSF events were post-glacial. If the rock-slope failures were deposited supra-glacially, they would have been transported down valley to form moraine ridges with characteristically uniform boulder lithology, as observed by Schleier et al. (2015). Such discontinuous rock-avalanche deposits are very distinctive from intact CRSF lobes deposited in an ice-free valley. In the Romsdal Valley no analogue moraine ridges were observed, and all our CRSF deposits under the Mannen instability form continuous lobate landforms with clear runouts into or across the valley.

Stratigraphic observations (Fig. 4) help constraining the timing of CRSF Lobe 1. While boulders from the Lobe 1 event overlie sandy to gravelly stratified drift (FA I), fine-grained stratified sediments (FA IV) also cover the bouldery CRSF material at this location (GPR; Fig. 5). The deltaic foreset structures of RU II are observed at the same elevation as the chaotic CRSF structures, which lie downriver of RU II and seem to "truncate" the delta. Both units are covered by the bank overflow sediments (FA/RU IV). The relative stratigraphy of these units narrows the failure timing for CRSF Lobe 1 to between 12 ka, when the valley became ice free, and 10.5 ka, when the coastline dropped below the recent riverbed of 50 m a.s.l. (Fig. 7). Observations of abandoned erosional channels through the CRSF deposits several meters above today's river level supports this interpretation.

[Fig. 7]

The adjacent CRSF deposit (Lobe 2) is the oldest of our dated events with an apparent exposure age of 9.39 ± 0.64 ka (Table 2). The approximated sea-level curve after Svendson and Mangerud

(1987) indicates that the location was effectively above sea-level 11 ka ago (Fig. 7A). The age therefore may represent the time of failure and not the timing of sea-level drop. According to the morphology in the DEM, it is possible that this deposit underlies CRSF Lobe 1, which would mean that the real age lies in the upper range of the uncertainties and has thus been deposited into a shallow fjord or high river level, shortly after deglaciation.

To identify CRSF Lobe 3, we had to rely on the high resolution DEM and relief analysis, as the deposit is hardly distinguishable from the surrounding landforms. In most places, it could only be mapped by the characteristic chaotic boulder fields covering the surface. This indicates that the deposits have been modified by the same erosional processes, as the underlying sediments. We therefore suggest that this deposit is older or the same age as CRSF Lobe 1 and 2. Thus, according to the regional deglaciation, the composite stratigraphy and morphology, the reconstructed curve of sea-level drop and the TCN ages, we can place three CRSF events (Lobes 1-3) from Mannen into a 2000 year time period between 12 ka and 10 ka ago.

Ten of our thirteen ^{10}Be ages fall into the time range of 4.5-5.5 ka (Fig. 7C) considering their external errors. The overlapping ages of the different deposits indicate that there have been several failures from the same slope within a couple of hundred years at most, witnessing a "geological crisis" during this time period. Based on the morphology, it is not clear if the deposits 4a-c are only one or up to three individual events. The same applies for the CRSF deposits 6a and 6b. The "geological crisis" thus included three to six failures from the same slope. The phenomenon of spatial rock-slope failure clusters and multiple failures from the same slope has been observed world-wide (Orwin et al., 2004; Jarman et al., 2014). In Norway this has happened at the Loen site, which has failed repeatedly within a few decades in the early 20th century. Together with a large scale rock-slope failure in Tafjord, CRSF became the natural hazards in Norway with the highest death toll (Reusch, 1907; Grimstad and Nesdal, 1991; Hermanns et al., 2006a).

5.2. Possible conditioning for multiple CRSFs at Mannen

Some of the regional and local clusters of CRSF in the Karakoram, the Andes, the Alps and the Scottish Highlands are discussed to be conditioned by tectonic or isostatic uplift and related stresses and seismic activity (Hewitt et al., 2011; Hermanns and Strecker, 1999; Köpfli et al., 2017; Ballantyne et al., 2014). However, in regions with recent low seismicity, this connection is often ambiguous and temporal rock-avalanche clusters are also linked to climatic changes and increased precipitation (Sanchez et al., 2009; Zerathe et al., 2014). Studies about rock-avalanche clusters in the Alps suggest that lithology and the structural predisposition is the most important long-term control on rock-avalanching (Hermanns et al., 2006a; Ostermann and Sanders, 2017), while seismicity is often the trigger with climate conditions as a second order control.

The deposits at Mannen cluster not only in space but also in time, in contrast to many regional clusters where CRSFs seem to have happened throughout the Holocene with rather low recurrence intervals implying a relaxation of the rock slope after failure (Schleier et al., 2015, 2016). This compares with the increasing number of studies globally which show that one slope of the same mountain can fail repeatedly within only a few years and decades (Plafker and Ericksen, 1978; Hermanns et al., 2001; McSaveney, 2002; Hermanns et al., 2004; Crosta et al., 2017). Hermanns et al. (2006b) argue that sudden stress release due to a failure causes a reorganisation of the stress field and can thus have a destabilising effect on the rock slope, which is in agreement with the structural simulations by Crosta et al. (2017).

In the Romsdal Valley, the regional clustering of CRSF within a geological unit supports the strong pre-conditioning based on the lithological and structural setting. Considering that neo-tectonic activity has so far not been demonstrated in western Norway, the relatively short recurrent interval indicates that driving factors other than tectonic activity may play a significant role in this region.

The age of the first three CRSF at the Mannen rock-slope instability closely post-dates the local deglaciation (12.8-11.7 ka) and coincides with the main peak of rock-avalanche activity in Norway (Böhme et al., 2015; Hermanns et al., 2017). Thus, sudden failure was most likely conditioned by the paraglacially-induced stress increases in the over-steepened slopes during and immediately following deglaciation.

The later timing of the mid Holocene cluster 5 ka ago invites for a speculation of how changing climate conditions in the Holocene may have contributed to these events. There are two main climatic factors which can contribute to Coulomb failure by decreasing effective shear strength owing to reduced coefficient of friction, increased pore-water pressure, increased slopes, and redistribution of centre of mass: (1) Regional precipitation changes (amount and type), and (2) temperature changes leading to changes in possible permafrost conditions. There is evidence from several studies in western Norway that a climatic deterioration initiated about 6 ka ago, after a the long warm period of the Holocene thermal optimum (HTO). Glacier growth (Nesje et al., 2001) and changing vegetation (Barnett et al., 2001) indicate a generally cooler and wetter climate in this period, and studies documenting Holocene debris flows, snow avalanches, and flooding events suggest a strong seasonality with severe winters and warm summers (Blikra and Nemec, 1998; Blikra and Selvik, 1998; Vasskog et al., 2011) at this time. Precipitation between 6 and 5 ka was 170% greater than during the reference period 1961-1990 (Bøe et al., 2006). Lilleøren at al. (2012) approximated the temperature anomalies based on published climate proxies for southern Norway for the last 10 ka compared to the same reference period (Fig. 7B), which was about 1˚C colder than mean annual air temperatures (MAAT) today. The MAAT during and after the HTO was warmer than during the reference period, with very mild winters and warm summers, driven by higher solar radiation due to the Earths orbital position. Cooling from 6 ka was most likely driven by low winter temperatures, while the summer temperatures decreased less extremely, reflecting a strong seasonality. The documented glacier growth

in southern Norway (Nesje et al., 2001) indicates additional high precipitation rates in winter after 6 ka ago. The timing of our geological crisis with at least three CRSF within a short period of time coincides with this period of strong winter temperature decrease, high precipitation rates and strong seasonality, following the HTO with high air temperatures.

Not much is known about the rock mechanics and the history of stream discharge and fluvial dynamics at Mannen. The mountain section seems to be generally very dry where no surface discharge is observed and precipitation and snow-melt water drains by baseflow through fractures underground. Continuous monitoring at the most active part of the Mannen instability "*Veslemannen*" reveals that rock mass deformation is very sensitive to precipitation and is stable during the winter season (Oppikofer et al., 2013). This could imply that increasing precipitation in the mid Holocene together with warm summer temperatures led to widespread and repeated rock-slope destabilisation at Mannen. A continued climate warming combined with a more pronounced seasonality leading to increased snow melt, could thus cause sudden destabilisation of the Mannen rock-slope in the future causing one or multiple CRSF events.

The other first order control is the regional degradation of permafrost during the HTO and after the 6 ka cooling period. Thermal measurements today in crevasses and the back scarp of the Mannen instability along with regional permafrost mapping indicates that Mannen is situated at the present mountain permafrost limit in the area (Westermann et al., 2013; Gisnås et al., 2013; Steiger et al., 2016). When the Mannen area became ice-free after the YD, the climate was 7-9°C cooler than today based on Greenland ice-core analysis (e.g. North Greenland Ice Core Project members, 2004). First approximations through a modelling approach suggests the build-up of several tens- to hundreds of meters of permafrost in mostly snow-free rock walls during the period of deglaciation until MAAT reached similar levels to today (ca. 10 ka ago) (Myhra et al., 2017). Rock joint weakening due to Permafrost aggradation and degradation during this 2 ka period after deglaciation may have played a role in addition to debuttressing for the first three CRSF at Mannen (Krautblatter et al. 2013). The permafrost certainly degraded during the HTO, but the degradation rate is depending on cracks and the ice content in the steep slopes because of thermal inertia. Thawing permafrost is widely recognised as an important factor for CRSFs (Fischer et al., 2006, 2012; Blikra and Christiansen, 2014) due to melting of ice-bonds in cracks and generally weakening of tensile and compressive strength in rock masses (Murton et al., 2006; Krautblatter et al., 2013), and has to be taken into account when discussing possible former rock slide conditioners in high-mountain environments. However, a more substantial conclusion on this can only be drawn through sensitivity studies using coupled thermo-mechanical models (Grämiger et al., 2017).

6. Conclusions

Below the Mannen instability in the lower Romsdal Valley, western Norway, a cluster of at least six post-glacial CRSF deposits complements a complex valley-fill stratigraphy. The present landforms are

the result of the concurrence of sedimentation processes connected to deglaciation, isostatic rebound and sea-level drop, and mass wasting from the slopes. Prominent steep steps in the relief, parallel to the valley, are evidence for erosional processes either by strong tidal currents or fluvial incision. These processes have modified both stratified drift and three of the rock-slope failure deposits, supporting the stratigraphically derived time constrains of failure timing.

A set of 13 exposure ages together with sedimentologic and morphologic analyses allowed for the age determination of the six to nine distinct CRSF events. They divide into two periods of CRSF activity, one shortly after deglaciation and one 5.5 to 4.5 ka ago, where multiple CRSF from the same slope occurred within a short period of time. The fact that one slope fails repeatedly with recurrence intervals of a few years or decades has been observed before and must be considered for future failure scenarios. Debuttressing is a probable conditioner for the early multiple failures between 12 and 10 ka, that coincide with a major peak in rock-avalanche activity in Norway. The timing of a mid Holocene cluster with three to six individual CRSF events has been connected to climate variation during the Holocene, especially in relation to a climatic deteoration at the end of the Holocene Climate Optimum. Higher precipitation connected to a strong seasonality, temperature changes and rock mass strength alterations related to permafrost degradation are possible climatic conditions responsible for the mid-Holocene crisis at Mannen.

7. Acknowledgments

The study is part of the project "CryoWALL – Permafrost slopes in Norway" (243784/CLE) funded by the Research Council of Norway (RCN). Additional funding was provided by the Norwegian Geological Survey, Trondheim, and the Department of Geosciences, University of Oslo. J. Gosse acknowledges support for the TCN laboratory from Canada Foundation for Innovation (21305 and 36158), NSERC, and NSRIT grants. The TCN sample preparation was mostly completed by the first author at CRISDal at Dalhousie University under supervision of G. Yang. Field assistance was provided by F. Magnin, B. Altena and S. Westermann (all University of Oslo) and B.R. Snook (NTNU). Discussions about the mapping investigations with R. Eilertsen, L. Rubensdotter and L. Hansen (all NGU) improved the study significantly. We thank G. Gilbert for reviewing and improving the manuscript significantly before submission and wish to thank S. Zerathe and two anonymous reviewers for their suggestions that allowed improving the former version of the manuscript.

References

Agliardi F, Zanchi A and Crosta, GB (2009) Tectonic vs. gravitational morphostructures in the central Eastern Alps (Italy): Constraints on the recent evolution of the mountain range. Tectonophysics 474, 250–270.

Aizebeokhai AP (2010) 2D and 3D geoelectrical resistivity imaging: Theory and field design. Sci. Res. Essays 5, 3592–3605.

Allen SK, Gruber S and Owens IF (2009) Exploring steep bedrock permafrost and its relationship with recent slope failures in the Southern Alps of New Zealand. Permafr. Periglac. Process. 20, 345–356.

Ballantyne CK, Sandeman GF, Stone JO and Wilson P (2014) Rock-slope failure following Late Pleistocene deglaciation on tectonically stable mountainous terrain. Quat. Sci. Rev. 86, 144–157.
Ballantyne CK and Stone JO (2013) Timing and periodicity of paraglacial rock-slope failures in the Scottish Highlands. Geomorphology 186, 150–161.
Ballantyne CK, Stone JO and Fifield LK (1998) Cosmogenic Cl-36 dating of postglacial landsliding at the Storr, Isle of Skye, Scotland. The Holocene 8, 347–351.
Barnett C, Dumayne-Peaty L and Matthews JA (2001) Holocene climatic change and tree-line response in Leirdalen, central Jotunheimen, south central Norway. Rev. Palaeobot. Palynol. 117, 119–137.
Blikra LH and Christiansen HH (2014). A field-based model of permafrost-controlled rockslide deformation in northern Norway. Geomorphology 208, 34–49.
Blikra LH, Longva O, Braathen A, Anda E, Dehls JF and Stalsberg K (2006) Rock slope failures in Norwegian fjord areas: examples, spatial distribution and temporal pattern. Landslides Massive Rock Slope Fail. 475–496.
Blikra LH, Majala G, Anda E, Berg H, Eikenæs O, Helgås G, Oppikofer T, Hermanns RL and Böhme M (2016) *Fare- og risikoklassifisering av ustabile fjellparti - Faresoner, arealhåndtering og tiltak*. Report for NVE Norway. Report no. 77–2016, September. [in Norwegian]
Blikra LH and Nemec W (1998). Postglacial colluvium in western Norway: depositional processes, facies and palaeoclimatic record. Sedimentology 45, 909–959.
Blikra LH and Selvik SF (1998). Climatic signals recorded in snow avalanche-dominated colluvium in western Norway: depositional facies successions and pollen records. The Holocene 8, 631–658.
Bøe A-G, Dahl SO, Lie Ø and Nesje A (2006). Holocene river floods in the upper Glomma catchment, southern Norway: a high-resolution multiproxy record from lacustrine sediments. The Holocene 16, 445–455.
Böhme M, Oppikofer T, Longva O, Jaboyedoff M, Hermanns RL and Derron M-H (2015) Analyses of past and present rock slope instabilities in a fjord valley: Implications for hazard estimations. Geomorphology 248, 464–474.
Clavero J, Sparks R, Huppert H and Dade W (2002) Geological constraints on the emplacement mechanism of the Parinacota debris avalanche, northern Chile. Bull. Volcanol. 64, 40–54.
Corner GD (2006) A Transgressive-Regressive Model of Fjord-Valley Fill: Stratigraphy, Facies and Depositional Controls. In: Dalrymple RW, Leckie DA and Tillman RW (eds) *Incised Valleys in Time and Space*. SEPM Special Publication no. 85, pp.161-178.
Cossart E, Braucher R, Fort M, Bourlès DL and Carcaillet J (2008) Slope instability in relation to glacial debuttressing in alpine areas (Upper Durance catchment, southeastern France): Evidence from field data and 10Be cosmic ray exposure ages. Geomorphology 95, 3–26.
Crosta GB, Hermanns RL, Dehls J, Lari S and Sepulveda S (2017) Rock avalanches clusters along the northern Chile coastal scarp. Geomorphology 289, 27–43.
Dortch JM, Owen LA, Haneberg WC, Caffee MW, Dietsch C and Kamp U (2009) Nature and timing of large landslides in the Himalaya and Transhimalaya of northern India. Quat. Sci. Rev. 28, 1037–1054.
Eilertsen R, Corner GD, Aasheim O, Andreassen K, Kristofferson Y and Ystborg H (2006) Valley-fill stratigraphy and evolution of the Målselv Fjord Valley, Northern Norway. In: Dalrymple RW, Leckie DA and Tillman RW (eds) *Incised Valleys in Time and Space*. SEPM Special Publication no. 85, pp.179-195.
Eilertsen RS, Corner GD, Aasheim O and Hansen L (2011) Facies characteristics and architecture related to palaeodepth of Holocene fjord-delta sediments: Facies characteristics and architecture. Sedimentology 58, 1784–1809.
Eilertsen RS, Corner GD and Hansen L (2015) Using LiDAR data to characterize and distinguish among different types of raised terraces in a fjord-valley setting. GFF 137, 353–361.

643 Evans SG and Clague JJ (1994) Recent climatic change and catastrophic geomorphic processes in
644 mountain environments. Geomorphology 10, 107–128.
645 Fischer L, Kääb A, Huggel C and Noetzli J (2006) Geology, glacier retreat and permafrost degradation
646 as controlling factors of slope instabilities in a high-mountain rock wall: the Monte Rosa east
647 face. Nat. Hazards Earth Syst. Sci. 6, 761–772.
648 Fischer L, Purves RS, Huggel C, Noetzli J and Haeberli W (2012) On the influence of topographic,
649 geological and cryospheric factors on rock avalanches and rockfalls in high-mountain areas.
650 Nat. Hazards Earth Syst. Sci. 12, 241–254.
651 Gisnås K, Etzelmüller B, Farbrot H, Schuler TV and Westermann S (2013) CryoGRID 1.0: Permafrost
652 Distribution in Norway estimated by a Spatial Numerical Model. Permafr. Periglac. Process.
653 24, 2–19.
654 Gosse JC and Phillips F (2001) Terrestrial in situ cosmogenic nuclides: theory and application. Quat.
655 Sci. Rev. 20, 1475–1560.
656 Grämiger LM, Moore JR, Gischig VS, Ivy-Ochs S and Loew S (2017) Beyond debuttressing: Mechanics
657 of paraglacial rock slope damage during repeat glacial cycles. J. Geophys. Res. Earth Surf. 122,
658 1004–1036.
659 Grimstad E and Nesdal S (1991) Loen rockslides. A historical review. In: Barton M and Stephansson W
660 (eds) *Rock Joints*. Rotterdam: Balkema, pp. 1–6.
661 Groover KD, Burgess MK, Howle JF and Phillips SP (2016) Electrical resistivity investigation of fluvial
662 geomorphology to evaluate potential seepage conduits to agricultural lands along the San
663 Joaquin River, Merced County, California, 2012-13. Report for the U.S. Geological Survey.
664 Report No. 2016–5172, Reston, Virgina.
665 Hansen L, Beylich A, Burki V, Eilertsen RS, Fredin O, Larsen E, Lysså A, Nesje A, Stalsberg K and
666 Tønnesen JF (2009) Stratigraphic architecture and infill history of a deglaciated bedrock
667 valley based on georadar, seismic profiling and drilling. Sedimentology 56, 1751–1773.
668 Hermanns R, Niedermann S, Ivy-Ochs S and Kubik P (2004) Rock avalanching into a landslide-dammed
669 lake causing multiple dam failure in Las Conchas valley (NW Argentina) ? evidence from
670 surface exposure dating and stratigraphic analyses. Landslides 1, 113-122.
671 Hermanns RL, Blikra LH, Naumann M, Nilsen B, Panthi KK, Stromeyer D and Longva O (2006a)
672 Examples of multiple rock-slope collapses from Köfels (Ötz valley, Austria) and western
673 Norway. Eng. Geol. 83, 94–108.
674 Hermanns RL, Fauqué L and Wilson CGJ (2015) ^{36} Cl terrestrial cosmogenic nuclide dating suggests
675 Late Pleistocene to Early Holocene mass movements on the south face of Aconcagua
676 mountain and in the Las Cuevas–Horcones valleys, Central Andes, Argentina. Geol. Soc. Lond.
677 Spec. Publ. 399, 345–368.
678 Hermanns RL and Longva O (2012) Rapid rock-slope failures, In: Clague JJ and Stead D (eds)
679 *Landslides*. Cambridge University Press, Cambridge, pp. 59–70.
680 Hermanns RL, Niedermann S, Garcia AV and Schellenberger A (2006b) Rock avalanching in the NW
681 argentine andes as a result of complex interactions of lithologic, structural and topographic
682 boundary conditions, climate change and active tectonics. In: Evans SG, Mugnozza GS, Strom
683 A and Hermanns RL (eds) *Landslides from Massive Rock Slope Failure*. Springer Netherlands,
684 Dordrecht, pp. 497–520.
685 Hermanns RL, Niedermann S, Garcia AV, Sosa Gomez J and Strecker MR (2001) Neotectonics and
686 catastrophic failure of mountain fronts in the southern intra-Andean Puna Plateau,
687 Argentina. Geology 29, 619.
688 Hermanns RL, Schleier M, Böhme M, Blikra LH, Gosse J, Ivy-Ochs S and Hilger P (2017) Rock-
689 avalanche activity in W and S Norway peaks after the retreat of the Scandinavian Ice Sheet,
690 In: Mikoš M, Vilímek V, Yin Y and Sassa K (eds) *Advancing Culture of Living with Landslides*.
691 Springer International Publishing, Cham, pp. 331–338.

692 Hermanns RL and Strecker M (1999) Structural and lithological controls on large Quaternary rock
693 avalanches (Sturzstroms) in arid northwestern Argentina. Geol. Soc. of Am. Bull. 111, 934-
694 948.
695 Hermanns RL, Trauth MH, Niedermann S, McWilliams M and Strecker MR (2000) Tephrochronologic
696 constraints on temporal distribution of large landslides in northwest Argentina. Geology 108,
697 35–52.
698 Hewitt K, Clague JJ and Orwin JF (2008) Legacies of catastrophic rock slope failures in mountain
699 landscapes. Earth-Sci. Rev. 87, 1–38.
700 Hewitt K, Gosse JC and Clague JJ (2011) Rock avalanches and the pace of the late Quaternary
701 development of river valleys in the Karakoram Himalaya. Geol. Soc. Am. Bull. 123, 1836-1850.
702 Høgaas F, Hansen L, Rinstad BI, Sveian H and Olsen L (2012) Database for registrering av marin grense
703 (MG) i Norge. Report for the Geological Survey of Norway. Report no. 2012.063, December.
704 Trondheim. [in Norwegian]
705 Holm K, Bovis M and Jakob M (2004) The landslide response of alpine basins to post-Little Ice Age
706 glacial thinning and retreat in southwestern British Columbia. Geomorphology 57, 201–216.
707 Hughes ALC, Gyllencreutz R, Lohne ØS, Mangerud J and Svendsen JI (2016) The last Eurasian ice
708 sheets - a chronological database and time-slice reconstruction, DATED-1. Boreas 45, 1–45.
709 Ivy-Ochs S and Kober F (2008) Surface exposure dating with cosmogenic nuclides. Quat. Sci. J. 57,
710 179–209.
711 Ivy-Ochs S, Martin S, Campedel P, Hippe K, Alminov V, Vockenhuber C, Andreotti E, Carugati G,
712 Pasqual D, Rigo M and Viganò A (2017) Geomorphology and age of the Marocche di Dro rock
713 avalanches (Trentino, Italy). Quat. Sci. Rev. 169, 188–205.
714 Jarman D, Calvet M, Corominas J, Delmas M and Gunnell Y (2014) Large-Scale Rock Slope Failures in
715 the Eastern Pyrenees: Identifying a Sparse But Significant Population in Paraglacial and
716 Parafluvial Contexts. Geogr. Ann. Ser. Phys. Geogr. 96, 357–391.
717 Jia H, Xiang W and Krautblatter M (2015) Quantifying rock fatigue and decreasing compressive and
718 tensile strength after repeated freeze-thaw cycles. Permafrost and Perigl. Process. 26, 368-
719 377.
720 Jia H, Leith K and Krautblatter M (in press) Path-Dependent Frost-Wedging Experiments in Fractured,
721 Low-Permeability Granite. Permafrost and Perigl. Process.
722 Korup O (2004) Geomorphometric characteristics of New Zealand landslide dams. Eng. Geol. 73, 13–
723 35.
724 Korup O, Densmore AL and Schlunegger F (2010) The role of landslides in mountain range evolution.
725 Geomorphology 120, 77–90.
726 Köpfli P, Grämiger L, Moore JR, Vockenhuber C and Ivy-Ochs, S (2017) The Oeschinensee rock
727 avalanche, Bernese Alpes, Switzerland: a co-seismic failure 2300 years ago? Swiss Journal of
728 Geosciences 111, 205-219.
729 Krautblatter M, Funk D and Günzel FK (2013) Why permafrost rocks become unstable: a rock-ice-
730 mechanical model in time and space. Earth Surf. Process. Landf. 38, 876–887.
731 Krautblatter M and Leith K (2015) Glacier- and permafrost-related slope instabilities. In: Huggel C,
732 Carey M, Clague JJ and Kääb A (eds) *The high-mountain cryosphere. Environmental Changes*
733 *and Human Risks.* Cambridge University Press, Cambridge, pp. 147-165.
734 Leith K, Moore JR, Amann F and Loew S (2014) In situ stress control on microcrack generation and
735 macroscopic extensional fracture in exhuming bedrock. Journal of Geophysical Research-
736 Solid Earth 119, 594-615.
737 Lilleøren KS, Etzelmüller B, Schuler TV, Gisnås K and Humlum O (2012) The relative age of mountain
738 permafrost — estimation of Holocene permafrost limits in Norway. Glob. Planet. Change 92–
739 93, 209–223.

Longva O, Blikra LH and Dehls JF (2009) Rock avalanches: distribution and frequencies in the inner part of Storfjorden, Møre og Romsdal County. Report for the Geological Survey of Norway. Report no. 2009.002, 15. March. Trondheim. [in Norwegian]

Lønne I (1995) Sedimentary facies and depositional architecture of ice-contact glaciomarine systems. Sediment. Geol. 98, 13–43.

McSaveney MJ (2002) Recent rockfalls and rock avalanches in Mount Cook National Park, New Zealand. In: Evans SG and Degraff JV (eds) *Catastrophic landslides*. Geological Society of America.

Moreiras SM, Hermanns RL and Fauqué L (2015) Cosmogenic dating of rock avalanches constraining Quaternary stratigraphy and regional neotectonics in the Argentine Central Andes (32° S). Quat. Sci. Rev. 112, 45–58.

Murton JB, Peterson R and Ozouf J-C (2006) Bedrock fracture by ice segregation in cold regions. Science 314, 1127–1129.

Myhra KS, Westermann S and Etzelmüller B (2017) Modelled Distribution and Temporal Evolution of Permafrost in Steep Rock Walls Along a Latitudinal Transect in Norway by CryoGrid 2D. Permafr. Periglac. Process. 28, 172–182.

Nagelisen J, Moore JR, Vockenhuber C and Ivy-Ochs S (2015) Post-glacial rock avalanches in the Obersee Valley, Glarner Alps, Switzerland. Geomorphology 238, 94–111.

Nesje A, Matthews JA, Dahl SO, Berrisford MS and Andersson C (2001) Holocene glacier fluctuations of Flatebreen and winter-precipitation changes in the Jostedalsbreen region, western Norvay, based on glaciolacustrine sediment records. The Holocene 11, 267–280.

NGU (2018) Kvartærgeologiske Kart (Løsmassekart). Available at: http://geo.ngu.no/kart/losmasse/ (accessed 17 April 2018). [in Norwegian]

North Greenland Ice Core Project members (2004) High-resolution record of Northern Hemisphere climate extending into the last interglacial period. Nature 431, 147.

NVE (2018) NVE Atlas. Available at: https://atlas.nve.no/Html5Viewer/index.html?viewer=nveatlas# (accessed 13 February 18). [in Norwegian]

Oppikofer T, Saintot A, Otterå S, Hermanns RL, Anda E, Dahle H and Eiken T (2013) Investigations on unstable rock slopes in Møre og Romsdal - status and plans after field surveys in 2012. Report for the Geological Survey of Norway. Report no. 2013.014, 13. November. Trondheim. [in Norwegian]

Orwin JF, Clague JJ and Gerath RF (2004) The Cheam rock avalanche, Fraser Valley, British Columbia, Canada. Landslides 1, 289–298.

Ostermann M and Sanders D (2017) The Benner pass rock avalanche cluster suggests a close relation between long-term slope deformation (DSGSDs and translational rock slides) and catastrophic failure. Geomorphology 289, 44–59.

Ostermann M, Ivy-Ochs S, Diethard S and Prager C (2016) Multi-method (^{14}C, ^{36}Cl, $^{234}U/^{230}Th$) age bracketing of the Tschirgant rock avalanche (Eastern Alps): implications for absolute dating of catastrophic mass wasting. Earth Surf. Proc. and Landf. 42, 1110–1118.

Ostermann M, Sanders D, Ivy-Ochs S, Alfimov V, Rockenschaub M and Römer A (2012) Early Holocene (8.6ka) rock avalanche deposits, Obernberg valley (Eastern Alps): Landform interpretation and kinematics of rapid mass movement. Geomorphology 171–172, 83–93.

Ouimet WB, Whipple KX, Royden LH, Sun Z and Chen Z (2007) The influence of large landslides on river incision in a transient landscape: Eastern margin of the Tibetan Plateau (Sichuan, China). Geol. Soc. Am. Bull. 119, 1462–1476.

Palacky GJ (1988) Resistivity characteristics of geologic targets, In: Nabighian M (ed) *Electromagnetic Methods in Applied Geophysics, Theory: Investigations in Geophysics.* SEG Books.

Penna IM, Hermanns RL, Niedermann S and Folguera A (2011) Multiple slope failures associated with neotectonic activity in the Southern Central Andes (37 -37 30'S), Patagonia, Argentina. Geol. Soc. Am. Bull. 123, 1880–1895.

Plafker G and Ericksen GE (1978) Nevados Huascarán Avalanches, Peru, In: Voight B (ed) *Developments in Geotechnical Engineering, Rockslides and Avalanches, 1*. Elsevier, pp. 277–314.

Plug LJ, Gosse JC, McIntosh JJ and Bigley R (2007) Attenuation of cosmic ray flux in temperate forest. J. Geophys. Res. Earth Surf. 112.

Roberts D (2003) The Scandinavian Caledonides: event chronology, palaeogeographic settings and likely modern analogues. Tectonophysics 365, 283–299.

Saintot A, Dahle H, Derron M-H, Henderson I and Oppikofer T (2012) Large gravitational rock slope deformation in Romsdalen valley (Western Norway). Rev. Asoc. Geológica Argent. 69, 354–371.

Sanchez G, Rolland Y, Corsini M, Braucher R, Bourlès D, Arnold M and Aumaître G (2010) Relationships between tectonics, slope instability and climate change: Cosmic ray exposure dating of active faults, landslides and glacial surfaces in the SW Alps. Geomorphology 117, 1-13.

Schleier M, Hermanns RL, Gosse JC, Oppikofer T, Rohn J and Tønnesen JF (2016) Subaqueous rock-avalanche deposits exposed by post-glacial isostatic rebound, Innfjorddalen, Western Norway. Geomorphology 289, 117-133.

Schleier M, Hermanns RL, Rohn J and Gosse JC (2015) Diagnostic characteristics and paleodynamics of supraglacial rock avalanches, Innerdalen, Western Norway. Geomorphology 245, 23–39.

NVE, met.no and Kartverket (2018) seNorge. Available at: http://www.senorge.no/ (accessed 17 April 2018).

Soldati M, Corsini A and Pasuto A (2004) Landslides and climate change in the Italian Dolomites since the Late glacial. CATENA 55, 141–161.

Steiger C, Etzelmüller B, Westermann S and Myhra KS (2016) Modelling the permafrost distribution in steep rock walls. Nor. J. Geol. 96, 329-341.

Storms JEA, de Winter IL, Overeem I, Drijkoningen GG and Lykke-Andersen H (2012) The Holocene sedimentary history of the Kangerlussuaq Fjord-valley fill, West Greenland. Quat. Sci. Rev. 35, 29–50.

Stroeven AP, Hättestrand C, Kleman J, Heyman J, Fabel D, Fredin O, Goodfellow BW, Harbor JM, Jansen JD, Olsen L, Caffee MW, Fink D, Lundqvist J, Rosqvist GC, Strömberg B and Jansson KN (2016) Deglaciation of Fennoscandia. Quat. Sci. Rev. 147, 91–121.

Sturzenegger M, Stead D, Gosse J, Ward B and Froese C (2015) Reconstruction of the history of the Palliser Rockslide based on 36Cl terrestrial cosmogenic nuclide dating and debris volume estimations. Landslides 12, 1097-1106.

Svendsen JI and Mangerud J (1987) Late Weichselian and holocene sea-level history for a cross-section of western Norway. J. Quat. Sci. 2, 113–132.

Tønnesen JF (2009) Georadarmålinger ved Rønningen og Horgheim i Romsdalen for undersøkelse av løsmassetyper i dalbunnen under det ustabile fjellpartiet Mannen. Report for the Geological Survey of Norway. Report no. 2009.062, 11. November. Trondheim. [in Norwegian]

Topping DJ (1993) Paleogeographic reconstruction of the Death Valley extended region: Evidence from Miocene large rock-avalanche deposits in the Amargosa Chaos Basin, California. Geol. Soc. Am. Bull. 105, 1190–1213.

Trauth MH, Alonso RA, Haselton KR, Hermanns RL and Strecker MR (2000) Climate change and mass movements in the NW Argentine Andes. Earth Planet. Sci. Lett. 179, 243–256.

Tveten E, Lutro O and Thorsnes T (1998) Geologisk kart over Norge, berggrunnskart Ålesund, 1:250,000. Geological Survey of Norway.

Vasskog K, Nesje A, Støren EN, Waldmann N, Chapron E and Ariztegui D (2011) A Holocene record of snow-avalanche and flood activity reconstructed from a lacustrine sedimentary sequence in Oldevatnet, western Norway. The Holocene 21, 597–614.

Westermann S, Schuler TV, Gisnås K and Etzelmüller B (2013) Transient thermal modeling of permafrost conditions in Southern Norway. The Cryosphere 7, 719–739.

841 Zerathe S, Lebourg T, Braucher R and Bourlès D (2014) Mid-Holocene cluster of large-scale landslides
842 revealed in the Southwestern Alps by 36Cl dating. Insight on an Alpine-scale landslide
843 activity. Quat. Sci. Rev. 90, 106-127.
844 Zimmerman SR, Evenson EB, Gosse JC and Erskine CP (1994) Extensive Boulder Erosion Resulting
845 from a Range Fire on the Type-Pinedale Moraines, Fremont Lake, Wyoming. Quat. Res. 42,
846 255–265.
847
848

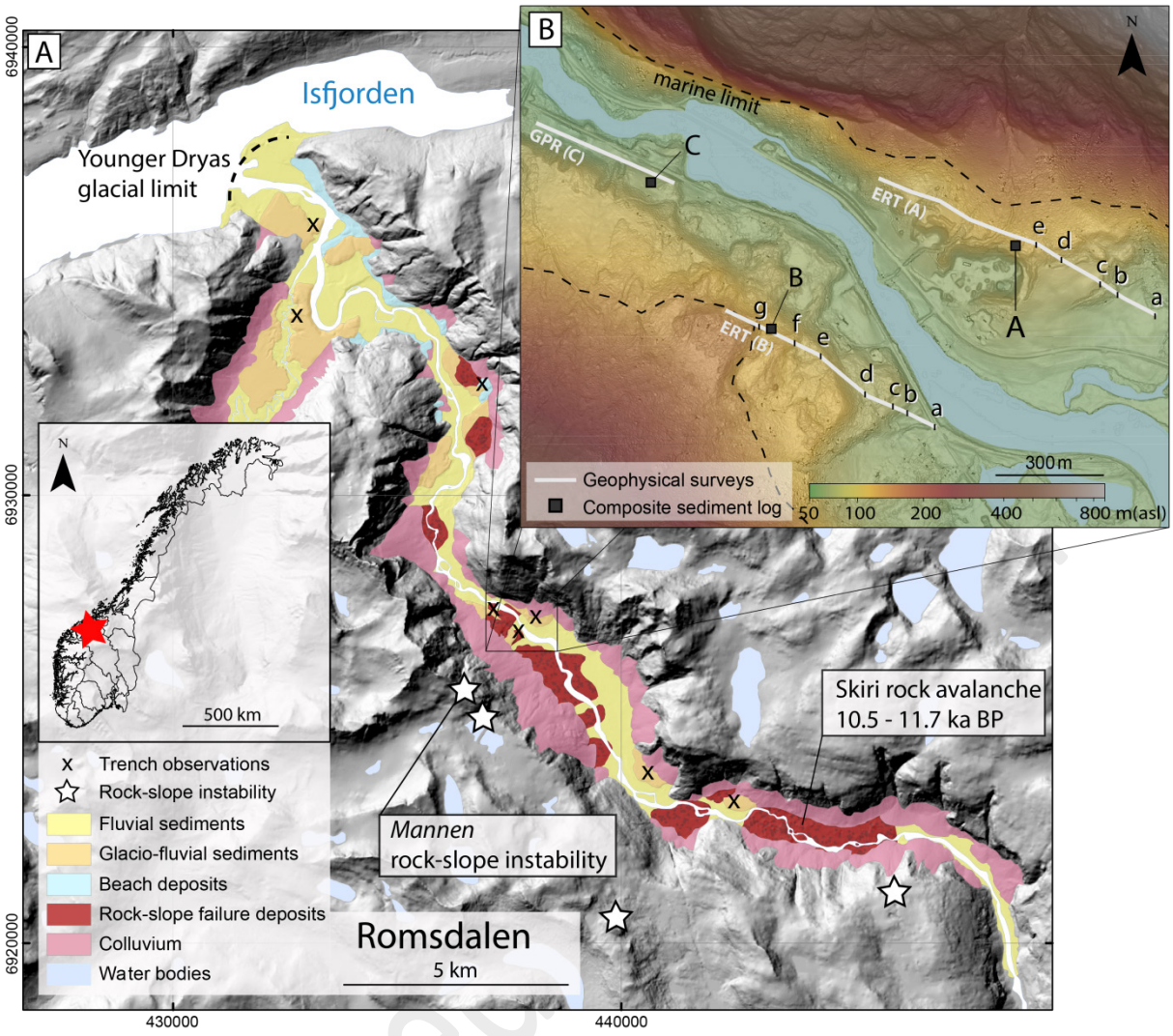

Figure 1: Overview over the study area: A) Quaternary geology of the lower and mid Romsdal Valley; B) detail of the main study site and the locations of geophysical surveys and composite sediment logs. Note the streched colour code.

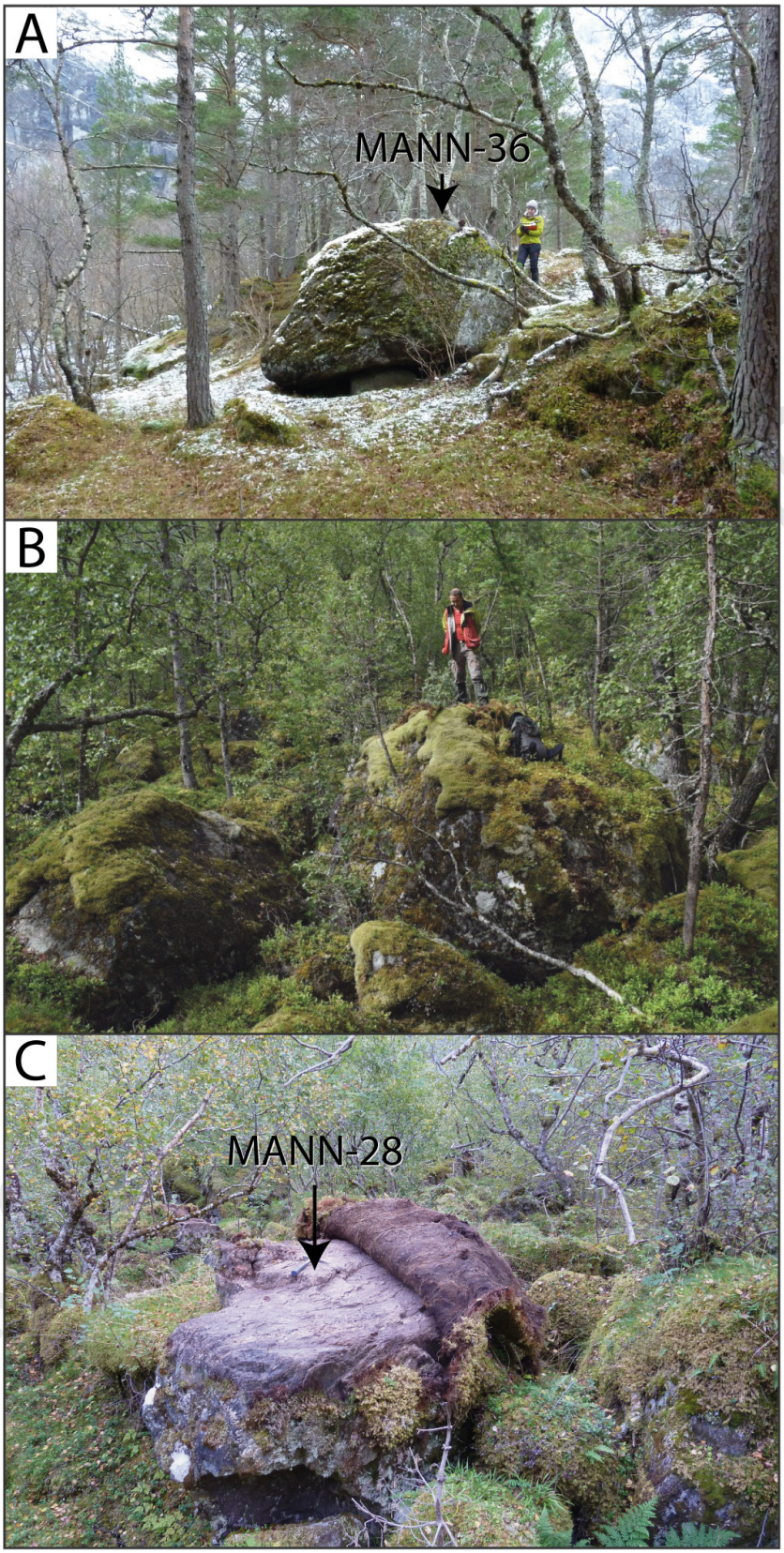

Figure 2: Images of A) the sample location MANN-36 in a surrounding characterised by soil in contrast to B) the chaotic boulder field of the south eastern CRSF deposits and C) the sample location MANN-28 with a pulled back moss cover.

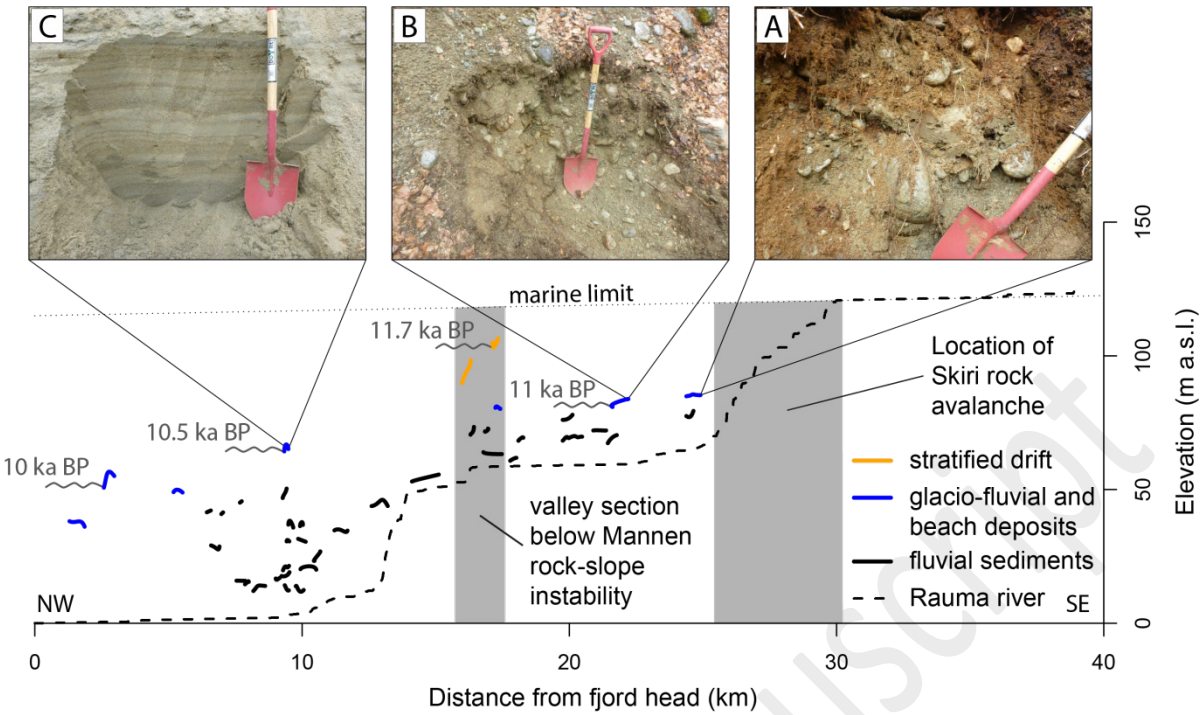

Figure 3: Surface profiles of terrace segments along the Romsdal Valley characterized according to their relative position and field observations (Photos A-C). Sea-level elevations and their approximate timing are indicated as waved gray lines next to the glacio-fluvial terace segments, which could be connected to a delta progradation. The vertical axis is exaggerated by 10 in relation to the horizontal axis.

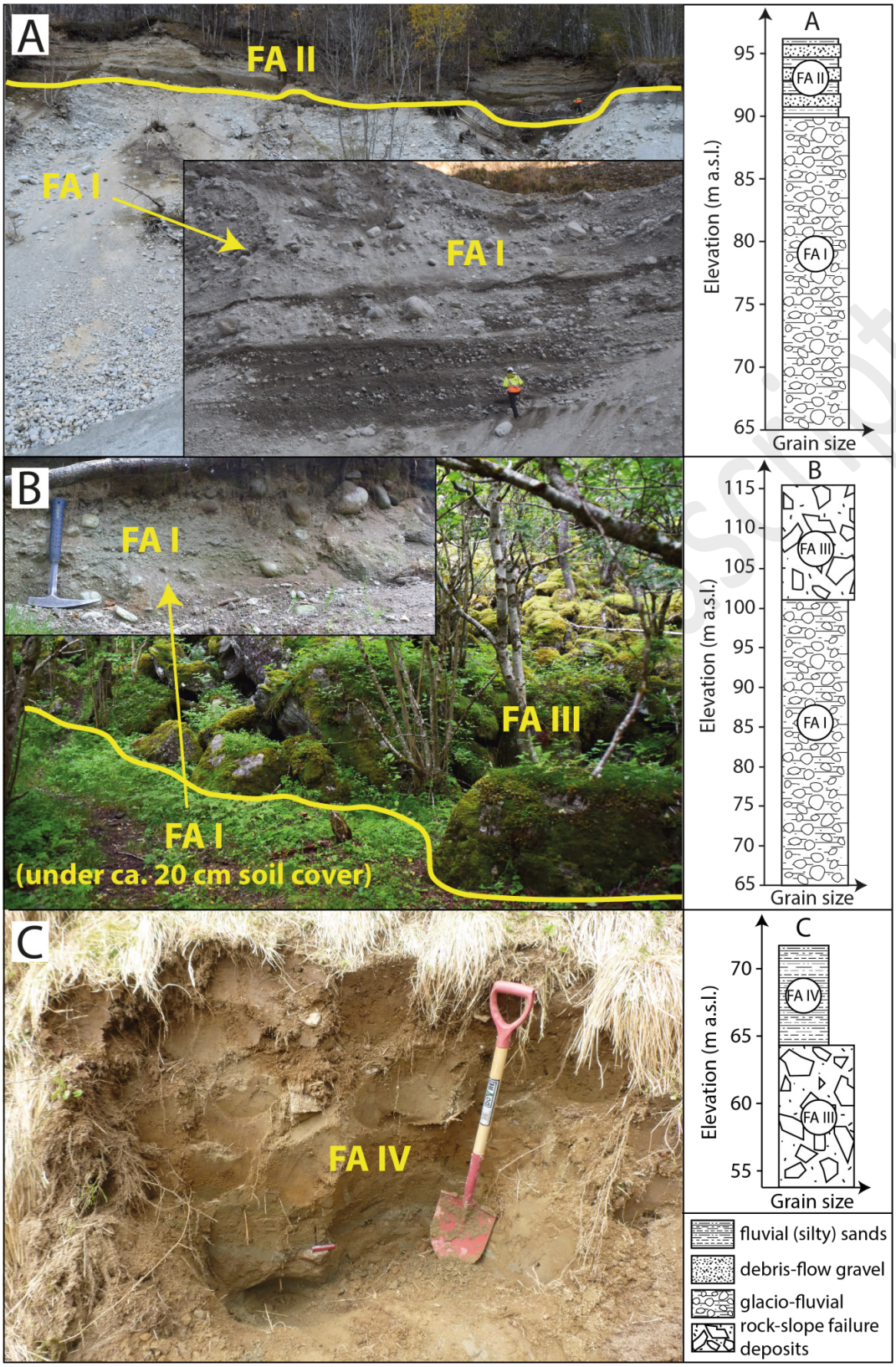

862

863 Figure 4: Impressions from the locations of the composite sediment profiles and the sediment
864 characteristics: A) Gravel pit with ca. 35 m stratified drift (FA I) and ca. 7 m interbedded fluvial sands in
865 angular debris-flow gravel (FA II), person is 1,70m tall; B) ca. 15 m thick chaotic boulder deposits (FA
866 III) on top of FA I, which is only visible in small outcrops; C) silty sands with outsized cobbles on top of
867 ca. 10m thick rock-slope failure boulders.

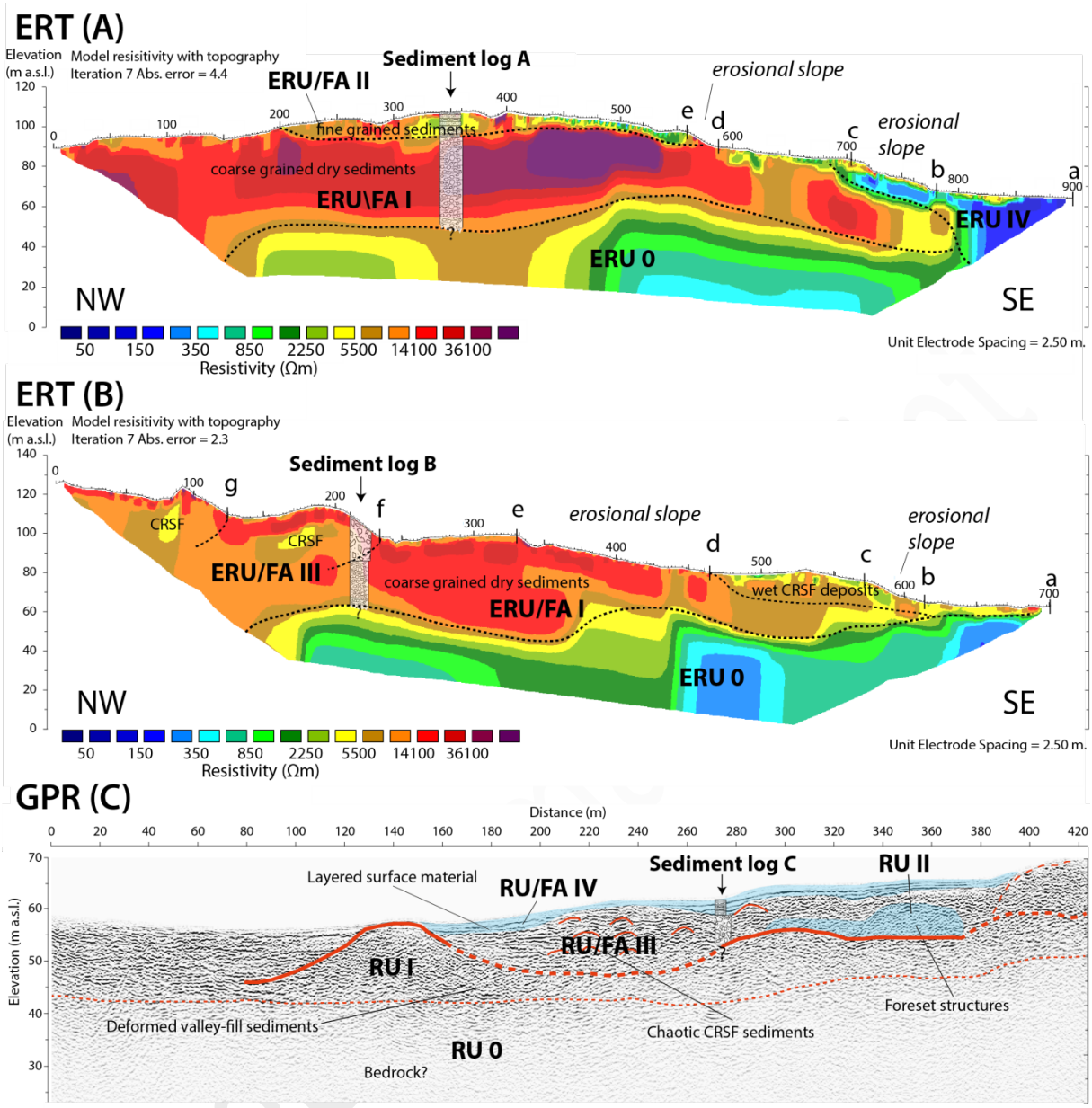

Figure 5: Results of the geophysical surveys: Top: 2D DC resistivity pseudosections of the profiles ERT (A) and ERT (B) (NW-SE) as indicated in figure 1B. The lowercased letters along the profiles represent prominent relief changes (Fig. 1B) that are connected to a change in sediment characteristics in places. Steep and ca. 20 m high steps in the relief are marked by the sections b-c and d-e, respectively. Bottom: GPR survey over CRSF deposits. Note that the scales differ for visualiasation. The y-axes are exaggerated by 1.5 in all profiles. The composite stratigraphy logs from figure 3 are included in the approximate locations.

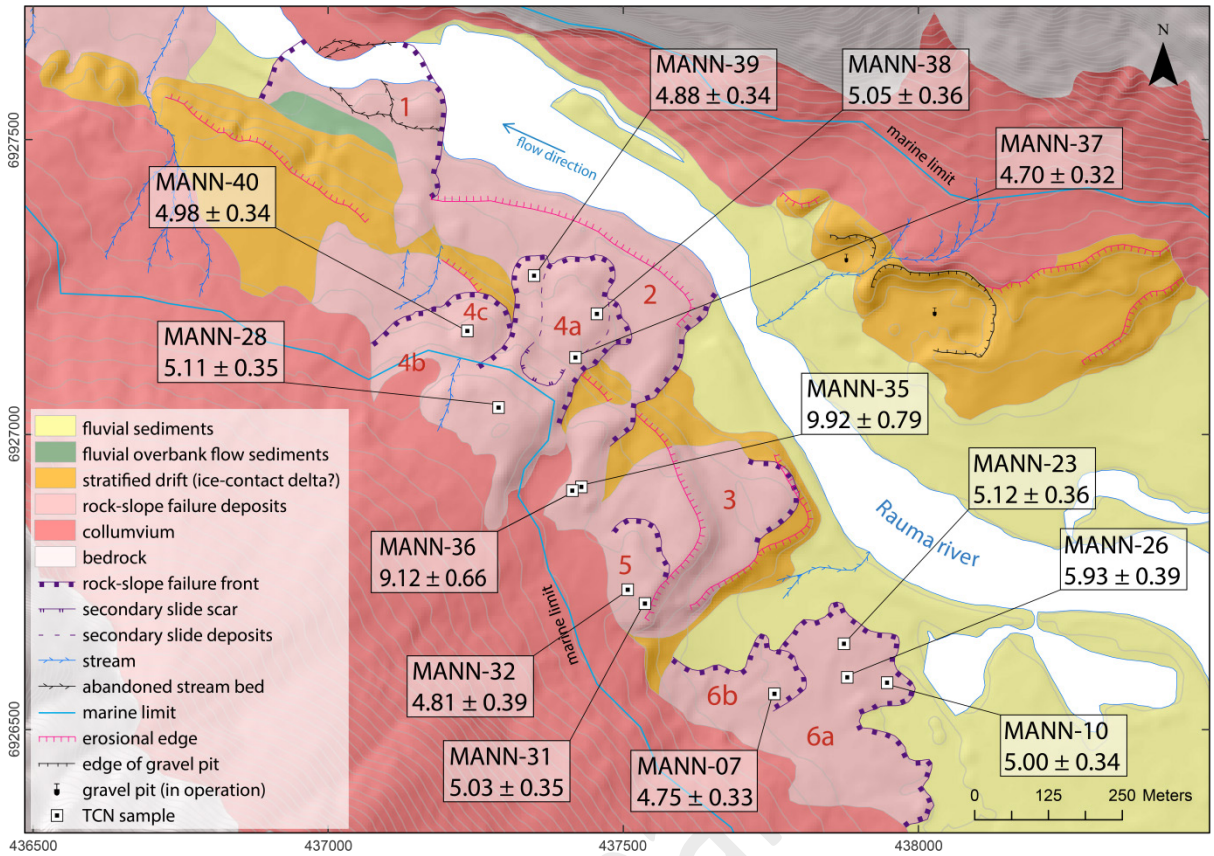

Figure 6: Quaternary geology map of the study site in the lower Romsdal Valley below the Mannen rock-slope instability. The individual apparent exposure ages are stated with 1σ uncertainties. The CRSF deposits are numbered for further discussions.

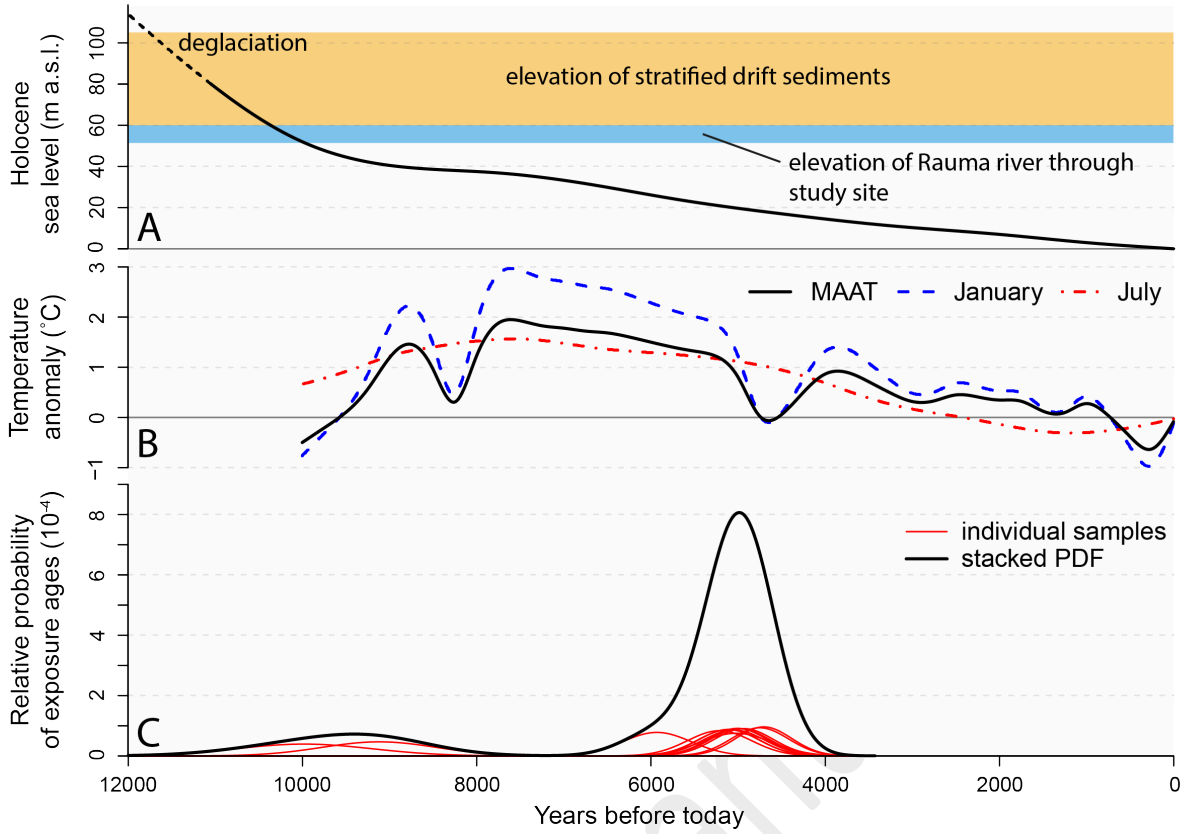

Figure 7: Local sea-level curve approximated after Svendsen & Mangerud (1987) (A) and approximated Holocene temperature anomalies for southern Norway (Lilleøren et al., 2012) (B) above apparent exposure ages as individual probability density functions (PDF) and stacked PDF (C).